Structure of the Atmosphere of Mars in Summer at Mid-Latitudes

ALVIN SEIFF AND DONN B. KIRK

Ames Research Center, NASA, Moffett Field, California 94035

The structure of Mars' atmosphere was measured in situ by instruments on board the two Viking landers from an altitude of 120 km to near the surface. The two entries were separated by 178° in longitude, 25° in latitude, 45 days elapsed time, and 6 hours in Mars local time. Atmosphere structure was very well defined by the measurements and was generally similar at the two sites. Viking 1 and 2 surface pressures and temperatures were 7.62 and 7.81 mbar and 238°K and 226°K, respectively, while pressures at the elevation of the reference ellipsoid were 6.74 and 6.30 mbar. Mean temperature decreased with a lapse rate of about 1.6°K/km, significantly subadiabatic, from above the boundary layer to about 40 km, then was near isothermal but with a large-amplitude wave superimposed, attributed to the diurnal thermal tide. The mean profile appears to be governed by radiative equilibrium. Differences between the two temperature profiles are due to diurnal effects in the boundary layer, a small cooling of the Viking 2 profile up to 40 km due to latitude and season, and effects of time of day, latitude, terrain, and season on the wave structure. The density data merge well with those of the upper-atmosphere mass spectrometer to define a continuous profile to 200 km. The temperature wave continues above 100 km, increasing in amplitude and wavelength.

INTRODUCTION

Knowledge of the structure of the neutral atmosphere of Mars has advanced rapidly in the age of space astronomy. Remote sensing experiments from flyby and orbiting spacecraft have indicated the mean surface pressure to be near 5 mbar, much lower than was previously accepted (see, for example, *Kliore et al.* [1972]), and in conjunction with ground-based spectroscopy have indicated that the atmosphere is predominantly CO_2. Remote sensing has also indicated that the temperature structure up to 45-km altitude is highly variable, dependent on latitude, season, and the dust content of the atmosphere [*Kliore et al.*, 1972; *Hanel et al.*, 1972].

The temperature data have been limited to the lowest 35 km (occultation) and 45 km (IR sounding) and have been somewhat puzzling and hard to assess because of their diversity. It has not been possible to say conclusively what accuracy, temperature resolution, and altitude resolution should be assigned to these results.

The USSR spacecraft Mars 6 made some measurements of the atmosphere structure during its entry into Mars in 1974 [*Kerzhanovich*, 1977]. Very useful information was obtained, although it was limited by the lack of direct temperature sensing, an extensive radio blackout, and acceleration sensing confined to four points. It confirmed the magnitude of the surface pressure obtained from remote sensing, measuring 5.45 ± 0.3 mbar, and put bounds on the temperature structure, indicating a lapse rate of 2.9°K/km up to 33 km and an isothermal middle atmosphere at 149° ± 8°K to 90 km in early spring in the southern hemisphere (−24° latitude). There was significant uncertainty in temperatures below 30 km, with a maximum of ±18° at 29 km.

The Viking mission provided an opportunity for in situ measurements of the atmosphere, and experiments to make use of that opportunity were described by *Nier et al.* [1972]. The atmosphere structure measurement approach, initially proposed in 1962 [*Seiff*, 1963], was the subject of intensive study and development in the ensuing 9 years, culminating in a test flight of the experiment in the earth's atmosphere in 1971. This experiment showed that the techniques for measuring the atmosphere during high-velocity entry were capable of providing data of comparable quality to that normally obtained from meteorological sounding techniques [*Seiff et al.*, 1973]. A description and discussion of the techniques and instruments which have been applied to the Viking mission has been given [*Seiff*, 1976].

This paper reports the results of the atmosphere structure measurements from Viking 1 and 2 as of May 1977. The analysis of the data is not yet complete in all respects, but we expect that the material we present herein will be substantially unchanged by further analysis. Two topics not yet ready for reporting are omitted—data on the winds encountered during entry and descent of the two landers and data on the terrain under the entry trajectories. These will be the subject of later reports. Preliminary accounts of the atmospheric data have been given [*Nier et al.*, 1976; *Seiff and Kirk*, 1976].

INSTRUMENT DESCRIPTION

The overall definition of the structure of Mars' atmosphere to be described herein was a result of synthesis of data from several instruments. In the upper regions of the experiment, altitudes from 120 to 26 km, a set of three-axis accelerometers measured the atmospheric density as a function of altitude from the vehicle deceleration. To calibrate this measurement, a thorough and extensive ground test program was conducted to define the drag coefficient as a function of velocity and Reynolds number in an atmosphere of CO_2. These tests were made with models of the Viking entry configuration in free flight through a ballistic range.

During parachute descent, which began nominally at 6 km, pressure and temperature were directly measured. Also throughout the high-speed entry the flow stagnation pressure was measured, and below about 25 km the flow recovery temperature (a temperature closely related to stagnation temperature) was directly sensed.

The lander sytems provided three kinds of data which were important to the determination of atmosphere structure: (1) altitudes, from a radar altimeter; (2) attitude change data, from gyroscopes, which were used in the determination of the trajectories and for analysis of wind effects; and (3) velocity data during parachute descent, from a three-axis Doppler radar.

The nominal measurement altitudes, telemetry resolution,

Copyright © 1977 by the American Geophysical Union.

Paper number 7S0499.

TABLE 1. Viking Atmosphere Structure Instruments

Sensors	Measurement Altitudes, km	Telemetry Resolution	Sample Interval, s	Altitude Resolution, km
Accelerometer	120–0	$\Delta V = 0.0127$ m/s	0.1	0.006–0.1
Pressure				
Aeroshell*	90–6	0.16 and 0.74 mbar	0.2	0.01–0.5
Parachute†	4.5–1.5	0.085 mbar	0.5	0.03
Temperature				
Aeroshell	27–6	1.2°K	1.0	0.01–0.1
Parachute	3.8–1.5	1.2°K	0.5	0.03
Radar altimeter	132–0	5 m	0.2	0.01–0.2
Doppler radar (TDLR)	5–0	0.06 m/s	1.0	0.012
Gyros	250–0	0.0008°	0.1	0.006–0.1

*The aeroshell phase of the experiment is from entry to nominally 6-km altitude.
†The parachute phase is from 6 km to descent engine ignition at 1.5 km.

sampling intervals, and altitude resolution of all these measurements are shown in Table 1. These were generally more than adequate for atmospheric definition. The accuracy of definition of temperature and pressure gradients with altitude in the parachute descent was constrained by telemetry resolution, as discussed below, but it was possible to define these gradients to the order of 1% or 2% on pressure and to within 0.1°K/km on temperature, or better.

The locations of the sensors on the landers are shown in Figure 1. The accelerometers and gyros were located within the inertial reference unit, external to the lander body, along the z axis, which was in the nominally vertical plane, pointing obliquely upward. These sensors were retained with the lander through the landing and provided necessary guidance data as well as scientific data on the atmosphere.

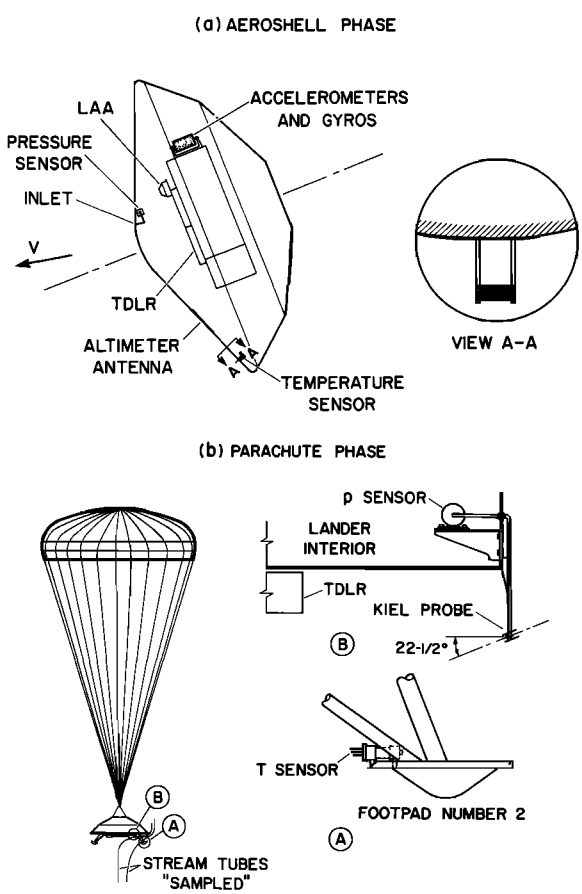

Fig. 1. Location of atmosphere structure instruments on the Viking landers. (*a*) The configuration of the spacecraft at atmosphere entry. (*b*) The instruments on the landers after heat shields were jettisoned and parachutes were deployed at a nominal altitude of 6 km.

The pressure inlet during high-speed entry was at the nominal flow stagnation point on the heat shield at the entry attitude. The aeroshell temperature sensor was deployed at a velocity of 1.1 km/s through the surface of the conical heat shield to a position safely outside the aeroshell boundary layer, where it could sense the atmospheric recovery temperature, without convective influence by the heat shield.

The pressure inlet during parachute descent was mounted on an edge of the lander body, with a Kiel probe geometry facing into the theoretical flow direction at that location (Figure 1*b*). This insured that the stagnation pressure was sensed. The temperature sensor in this phase was mounted on the inboard edge of the footpad on landing leg 2, where it sampled the temperature of oncoming stream tubes well away from thermal contact with the lander. This location also ensured a vigorous flow over the sensing elements at essentially the descent velocity.

The location of the Doppler radar (terminal descent and landing radar (TDLR)) on the lander bottom is also indicated. Two altimeter antennas were provided, one on the surface of the heat shield, used during high-speed entry, and the other on the lander bottom (LAA), used during parachute descent.

The acceleration sensors were derived from guidance quality accelerometers manufactured by Bell Aerospace Company (Bell model IX). They sense acceleration by electromagnetically constraining a test mass to a precise null position. The restoring force is provided by a current flowing in a coil mounted in the test mass, which reacts against the field of a permanent magnet in the sensor. The nulling current is the measure of the acceleration. The scale factor accuracy achieved is believed to have been better than 0.02%, with bias uncertainties <100 μg.

The temperature sensors were multiple fine wire (0.0127-cm diameter) thermocouples, directly exposed to the atmospheric flow. They were designed to minimize errors due to spurious inputs (radiation, conduction, etc.) by maximizing thermal coupling to the atmosphere. Response times were typically ~0.3 s in the aeroshell phase and 0.8 s in parachute descent. Reference junction temperatures were measured with platinum resistance thermometers, within the sensor housing.

The pressure sensors were thin stretched stainless steel diaphragms referenced to vacuum. Diaphragm displacement is the measure of the applied pressure. Unsupported diameters of the diaphragms were ~2.5 cm. Sensor characteristics are given in Table 2. In a thorough preflight test evaluation the sensors

TABLE 2. Pressure Sensors

Mission Phase	Range, mbar	Repeatability	Displacement Sensing
Aeroshell	0–150	±0.5% rdg	capacitive
	0–20	±0.5% rdg	capacitive
Parachute	0–18	±0.01 mbar	inductive

were found to be stable through the flight environments including prelaunch sterilization and launch and entry vibration. The sensor temperatures were nearly constant during entry and descent. Data were corrected for the effects of temperature on calibration where appropriate.

The design philosophy, development, and accuracy evaluation programs for all these sensors have been described in detail elsewhere [*Seiff*, 1976]. Some remarks on the accuracies achieved by the actual sensors during Mars entry will be incorporated into the discussions of results below.

Atmospheric Measurements During Parachute Descent

The two Viking landers deployed parachutes at altitudes of 5.80 and 5.92 km above the terrain. Parachutes were fully open at 5.60 and 5.63 km, and the heat shields were jettisoned at 5.03 and 4.96 km. This exposed the parachute phase pressure sensors to the atmosphere, but there was some interference with both pressure and altitude data by the departing heat shield, down to an altitude of about 4.5 km. The temperature sensors, on the footpad of lander leg 2, were deployed at altitudes near 3.9 km. From there until the terminal descent rocket engines were ignited, at about 1.45 km, both landers transmitted good-quality data on pressure and temperature of the atmosphere (Figures 2 and 3).

Only a small fraction of the data points received are shown, because many repetitions occurred at every digital level. Corrections made for dynamic pressure and temperature effects are indicated and will be discussed. These were of the order of 0.2 mbar and 1.5°K.

Below 1.45 km the descent rockets clearly affected the measurements, and no quantitative use was made of the data. The effect on measured pressures was, surprisingly, to lower them to a level very near ambient. The jets aspirated the region beneath the landers. In further detail the atmospheric pressure provides a boundary condition for the rocket jets, and the jets block atmospheric flow from impinging on the lander bottom and hence suppress dynamic effects on the pressure measurement. It is evident that pressures measured then were within 0.1 or 0.2 mbar of ambient. The effect on temperatures sensed was to raise them abruptly, presumably a result of mixing of the rocket effluent with the local atmosphere.

Pressure Measurements and Landing Site Elevations

Pressure was sampled during descent at 0.5-s intervals, corresponding to nominally 30 m in altitude. The telemetry resolution was 0.085 mbar. There were typically 6–8 repetitions of the reading at every digital level, of which only the first are plotted in Figure 2. These points have just surmounted, and hence are very close to, the reading level. It can be shown that the effective resolution under these circumstances is the nominal resolution/n, where n is the number of reading repetitions at the given level. Thus the effective resolution was about 0.014 mbar. The curves are put through the highest data points, since with pressure rising the resolution error is always negative. By this combination of practices the uncertainty in the relative pressure levels due to resolution was reduced to the order of 0.01 mbar. However, the uncertainty in the absolute pressure level is up to 0.085 mbar because of resolution uncertainty in the zero reading.

The zero readings of the sensors taken just before atmosphere entry established the zero readings for the measurement period. For both landers the sensors read a consistent zero level without deviation over a period of several hundred seconds prior to the actual pressure rise, and these readings differed by 0.10-mbar equivalent for Viking 1 and 0.027 mbar

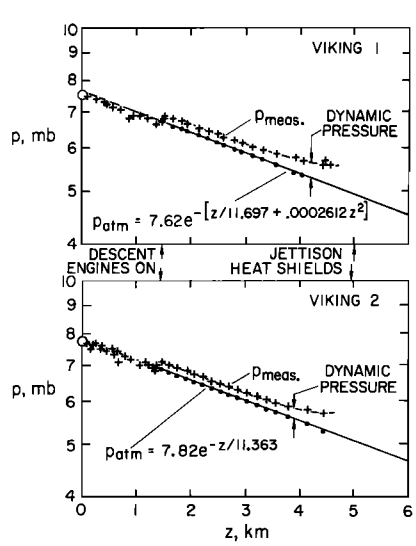

Fig. 2. Pressures measured during parachute descent. Dynamic corrections are indicated. The equations define the variation of atmospheric pressure with altitude in the parachute phase.

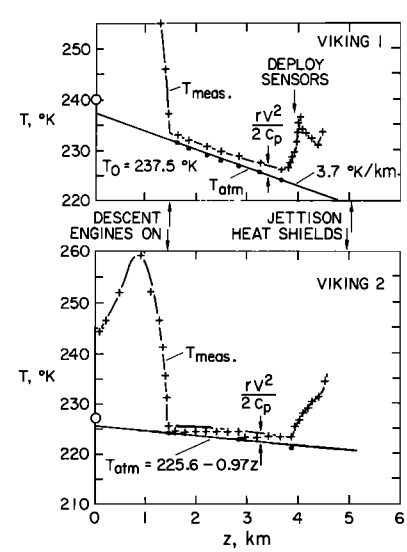

Fig. 3. Atmospheric temperatures; direct sensing in the lowest 5 km. Dynamic corrections are of the order of 2°K. The altitude of full deployment of lander leg number 2, on which the sensor was mounted, can be readily identified.

for Viking 2 from those obtained in calibration in July–November 1974. The repeatability of sensor scale factors, from data taken over the course of 4 months during the preflight test program in which the sensors were exposed to vibration, thermal cycling, etc., was better than 0.2% or 0.01 mbar at 5 mbar. The Viking 2 sensor calibrations were independent of sensor temperature within the data scatter. For Viking 1, scale factor changed by 0.018%/°C, which, for 10° uncertainty in sensor temperature during the measurement period, would lead to 0.01-mbar error at 5 mbar. Overall, we believe the errors due to calibration uncertainties to be within 0.01–0.02 mbar.

The dynamic pressure correction $\frac{1}{2}\rho V^2$ proceeds iteratively with the density initially defined from the uncorrected pressure. The correction accuracy is estimated to be 0.004 mbar. Lander descent velocities on the parachute were between 50 and 90 m/s. Dynamic pressure corrections were applied to the individual data points, prior to the defining of the curve $p_{atm}(z)$, and the corrected data are shown by the heavy dots in Figure 2.

For Viking 2 the plot of log p versus z was highly linear, consistent with the isothermal character of the lowest 4 km of the atmosphere. For Viking 1 a linear fairing also represented the pressure data very well. For both sets of data, however, a curve of the form

$$p/p_0 = \exp(-z/H_0 - k_2 z^2)$$

was defined to represent the curvature in the log $p(z)$ plot and to merge smoothly with the lowest few pressures obtained from the accelerometry near 30-km altitude. The values of surface pressure p_0 defined by simple logarithmic extension of the data between 1.5 and 4.0 km were 7.64 mbar for Viking 1 and 7.81 mbar for Viking 2. The values defined by nonisothermal fits were 7.62 and 7.80 mbar, respectively. The recommended values are 7.62 and 7.81 mbar, since Viking 2 was indeed very close to isothermal below 4 km.

The fitted equations had rms deviations from the data points of the order of 0.003–0.007 mbar, implying a high relative accuracy in the measured pressures. Since relative accuracy was important for defining the slopes dp/dz used in determining the mean molecular weight, pressures are stated in Table 3 to the nearest 0.001 mbar. It must be understood that only relative accuracy is implied, since absolute accuracy is limited by telemetry resolution of the zero reading. The maximum absolute uncertainty is 0.085 mbar, and the expected average uncertainty is 0.04 mbar in a large population of measurements.

Pressures measured after landing on sol 1 at the same time of day by the same sensor were reported by the Viking Meteorology Team [*Hess et al.*, 1976*a*]. These points are shown by circular symbols at $z = 0$ in Figure 2. They are in satisfactory agreement, within the telemetry resolution, with those projected downward from the parachute phase data. The scale heights at ground level were determined from the pressure data to be 11.70 km (Viking 1) and 11.36 km (Viking 2). Equations for $p(z)$ suitable for use in the lowest 30 km (Viking 1) and the lowest 5 km (Viking 2) are given in Figure 2.

The pressure difference recorded between the two landing sites is the combined result of differences in elevation, season, and time of day. The elevations were best given by the radio determinations of the landed radii 3389.38 ± 0.08 and 3381.88 ± 0.22 km [*Michael et al.*, 1976] in relation to the equipotential reference ellipsoid radii at the landing coordinates 3390.87 ± 0.23 and 3384.33 ± 0.23 km, respectively [*Christensen*, 1975]. These data indicate landing site elevations relative to the reference ellipsoid of −1.49 ± 0.24 km (Viking 1) and −2.45 ± 0.32 km (Viking 2). (The relative accuracy of these two determinations should be significantly better than the absolute accuracy.) Thus the second lander came to rest 0.96 km lower than the first, relative to the equipotential surface. Pressures at the equipotential surface at the times of landing are determined from Figure 2 to be 6.74 mbar (Viking 1) and 6.30 mbar (Viking 2). The difference, 0.44 mbar, reflects primarily the seasonal reduction in surface pressure between the landings. The seasonal decrease reported (Viking Meteorology Team, private communication, 1977) was 0.56 mbar at the Viking 1 site. The effect of diurnal variations was significant at the Viking 1 site, the pressure at the time of landing being 0.12 mbar below the daily mean [*Hess et al.*, 1976*a*]. Subtracting this from the seasonal effect, 0.56 − 0.12, gives 0.44 mbar. Hence the measurements of pressure and of landing site elevation are consistent with the seasonal and diurnal variations seen in the Viking meteorology experiment.

Temperature

Selected points from the temperature data from Viking 1 and 2 are plotted in Figure 3. Since the sensors were read every 0.5 s and readings were repeated at every digital level (7–15 times on Viking 1), the effective resolution was ~0.1°K, compared to the telemetry resolution of 1.1°K. On Viking 2, which

TABLE 3. Lower Atmospheric State Properties From Direct Sensing

	Viking 1			Viking 2		
z, km	p, mbar	T, °K	ρ,* kg/m³	p, mbar	T, °K	ρ,* kg/m³
0	7.620†	237.3†	0.01680†	7.820†	225.6†	0.01813†
0.5	7.301†	235.5†	0.01622†	7.48†	225.1†	0.01738†
1.0	6.994†	233.7†	0.01565†	7.16†	224.6†	0.01667†
1.5	6.707	231.8	0.01513	6.853	224.0	0.01600
2.0	6.427	230.1	0.01461	6.564	223.6	0.01536
2.5	6.150	228.3	0.01409	6.282	223.1	0.01473
3.0	5.885	226.5	0.01359	6.015	222.6	0.01413
3.5	5.635	224.7	0.01312	5.747	222.1	0.01353
4.0	5.39	222.8	0.01265	5.483	221.6	0.01294
4.5	5.16	222.1†	0.01221	5.222	221.2†	0.01235

For Viking 1, H_0 = 11.697 km, μ = 44.36 ± 0.41; for Viking 2, H_0 = 11.363 km, μ = 43.36 ± 0.35.
*Calculated for μ = 43.49, R = 191.18 J/kg°K.
†Extrapolated.

encountered a nearly isothermal atmosphere below 4 km, the first 36 readings were at a common digital level, followed by 52 readings at the next level, and one reading at a third level, just before the retro-rockets were ignited. Every eighth one of these data points is shown in Figure 3, but only the first at each level was used to establish the lapse rate with an effective resolution of 0.02°K.

The sensor reference junctions were at 265° on Viking 1 and 263.7° on Viking 2. The sensors were automatically compensated for cold junction temperature by means of a resistance network employing a platinum resistance element, but a small residual correction was applied, as defined by the preflight calibration data. The calibration data were repeatable within ±0.1°C, and interpolation errors between the widely spaced calibration points are estimated to be less than 0.2°C.

The accuracy expected from these data had been extensively analyzed in advance of flight [*Seiff*, 1976] and was concluded to be ~1°K, after consideration of errors due to the electronics, response lag, conduction and radiation, calibration uncertainties, and error in the dynamic temperature corrections. The data presented are still subject to small refinements, of the order of 1°K overall, by application of corrections for small perturbations due to conduction and radiation. Lag and dynamic correction errors are presently ~0.1° or less.

The dynamic correction is given by $rV^2/2c_p$, where c_p is the specific heat at constant pressure of the atmosphere, $V^2/2c_p$ is the temperature increment from conversion of kinetic energy to thermal energy in the gas flow approaching the sensor, and r, the recovery factor, is the fraction of this energy actually experienced by sensors in laboratory calibrations in 6-mbar CO_2 flows. The fraction $r = 0.80$ for the nominal wire diameter Reynolds number (8.4) and Mach number (0.23) during parachute descent. The corrections to the individual data points range from 1.3° to 2.3°.

Straight lines put through these data points so as to pass through the highest corrected points and within the resolution uncertainty of all lower points indicate lapse rates of 3.7°K/km and 0.97°K/km and are shown in Figure 3. The difference is a diurnal effect, as will be discussed below. Surface temperatures are indicated.

The linear lapse rate defined by the lower two points from Viking 2 passes slightly above the third point. This indicates that the initial reading at the 223.3°K level would have been observed to a somewhat higher altitude with earlier leg deployment.

Ground level atmospheric temperatures obtained on the first day after landing, at the same Mars local time, from the meteorology temperature sensor are plotted as circular symbols on the T axis. Agreement is satisfactory but suggests a region of slightly increased lapse rate near the surface.

The steadiness of the temperature readings on both landers, evidenced by a complete lack of fluctuation in the data returned, indicates a thermally homogeneous atmosphere. Because the sensor response lag was 0.77 s (at 2.5 km), small fluctuations (~1°) of ~20-m scale could have occurred without detection.

Mean Molecular Weight

Mean molecular weights were determined from data given in Figures 2 and 3. The defining relationship is

$$\mu = -(R_u T/pg)\,(dp/dz) \qquad (1)$$

which is a generalization to a nonisothermal atmosphere of the expression

$$\mu = R_u T/gH \qquad (2)$$

where R_u is the universal gas constant, g is local acceleration due to gravity, and H is scale height. All planetary properties on the right side of these expressions were determined by measurements. The acceleration due to gravity determined from the accelerometers after landing was extended upward as $(R_0 + z)^{-2}$. The accuracy-determining factor is dp/dz, which could be defined only to within about 1% in the presence of the finite telemetry resolution.

The mean molecular weight from Viking 2 data was 43.34 ± 0.8%. This is the average of six values at 0.5-km altitude increments from 1.5 to 4.0 km. The largest deviations from the mean occurred at the end points, where dp/dz is less well determined. Without the two end points the mean value is $43.36^{+0.2\%}_{-0.4\%}$. The derivative was determined from the equations fitted to the pressure data, of the form $p/p_0 = \exp(-k_1 z - k_2 z^2)$, to accommodate pressures measured near 30 km (see below). The fits were both within 0.007-mbar rms, well within the accuracy of determination of pressure.

Since the Viking 2 parachute phase data were essentially isothermal, μ was also calculated from the isothermal relationship to obtain 43.82 at z = 2.5 km, T = 223.1°K, and g = 3.7252 m/s². This is slightly outside the scatter band of the more precise measurement.

The Viking 2 mean molecular weight agrees well with that derived from atmospheric composition data. The landed mass spectrometer has reported a mixture of CO_2 with 0.027 ± 0.003 mol fraction of N_2, 0.016 ± 0.003 mol fraction of Ar, and 0.0015 ± 0.0005 mol fraction of O_2 [*Owen and Biemann*, 1976], for which the mean molecular weight is 43.486 ± 0.066. The present measurement corresponds to a nitrogen fraction of 0.035 for argon fractions of 0.013–0.019.

Similar analysis of the Viking 1 data gave μ = 44.36 ± 1.0%, and a simple scale height analysis gave 44.21, about 2% higher than the Viking 2 and the mass analysis values. A considerable effort was made to understand this discrepancy. It could be due to accumulation of maximum possible errors in pressure and temperature. The measurement of T is accurate to ~0.4%, and while the molecular weight is insensitive to scale factor errors in pressure, since $\mu \sim p^{-1}\,dp/dz$, it is sensitive to bias errors in pressure, such as that due to the resolution uncertainty in the zero reading, which could be as large as 1.5%. Hence an accumulation of the maximum expectable errors could add up to 1.9%. Two other possible explanations for the discrepancy are (1) that the small dynamic corrections require further refinement for the effects of wind (a first-order correction for wind is already incorporated) and (2) that the definition of dp/dz has been affected by terrain slopes under the lander. During the descent from 3.5 to 1.5 km the lander was transported about 0.7 km horizontally by winds, and if terrain elevation changed by 40 m along this track, the mean molecular weight would be close to that expected from the other measurements. The necessary ground slope is 3.27°. It has been reported that the lander came to rest at an angle of 2.99°–3.6° [*Mutch et al.*, 1976], and the same source reports, 'The topography (around Viking 1) is gently rolling . . . . The nominal horizon is 3 km away; however, nearby hills obscure our view of large segments of the far horizon.' We may have detected this topography in our molecular weight analysis.

The molecular weight analysis has another significance. It shows the internal consistency of the measurements. Even including the extraneous effects of winds and terrain, the entire

set of measurements is consistent to within 1% or 2% in mean molecular weight.

Atmospheric Densities and Tabulated State Properties

The atmospheric densities computed from the pressure and temperature profiles for $\mu = 43.49$ are plotted in Figure 4 and listed in Table 3, together with the pressures and temperatures at 0.5-km intervals, scale heights, and mean molecular weights determined from the experiment.

ATMOSPHERE RECONSTRUCTED FROM ACCELEROMETER DATA

The determination of the density, pressure, and temperature of the Martian atmosphere from an altitude of about 120 km to an altitude of about 26 km depended primarily on data from accelerometers carried on board the entry vehicles. In its simplest sense the density of the atmosphere, ρ, is proportional to the acceleration along the flight path, $-a_s$, through the equation

$$\rho = -2ma_s/C_D A V_r^2 \tag{3}$$

where m is the vehicle mass, C_D the aerodynamic drag coefficient, A the vehicle cross-sectional area, and V_r the vehicle velocity relative to the atmosphere. The mass and reference area are known constants, and the velocity can be continually tracked from the on-board deceleration measurements.

The analytical approach used to define the vehicle trajectory from the measured accelerations by use of the equations of motion is described in Appendix A. This analysis yields the vehicle velocity and altitude as functions of time and uses the altimeter data as an input. The measured densities are coupled with the reconstructed altitudes, which differ somewhat from the measured altitudes because of variable terrain elevation and roughness, to define $\rho(z)$, from which $p(z)$ is derived under the assumption of hydrostatic equilibrium. From p, ρ, and μ the temperature profile is obtained through the equation of state.

In (3) the drag coefficient must be known precisely, since fractional errors in C_D are the negative equivalent of fractional errors in density. The drag coefficient was measured in a series of simulation flight tests in the laboratory, by the use of a ballistic range with an atmosphere of CO_2. Parameters simulated were model velocity, Reynolds number, gas composition, and, of course, model geometry [*Intrieri et al.*, 1977; P. F. Intrieri, personal communication, 1976]. These tests led to the

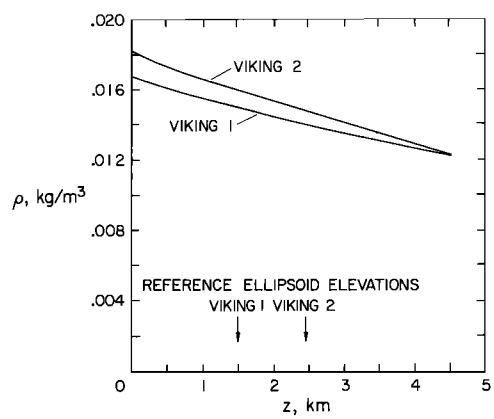

Fig. 4. Near-surface atmospheric densities above the Viking landing sites. Density at the reference ellipsoid was 0.015 kg/m³ at both landings.

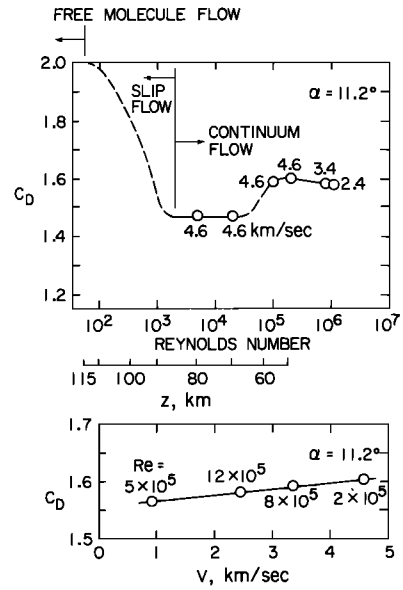

Fig. 5. Drag coefficients used to reconstruct the atmosphere. Test points are at velocity–Reynold number combinations which lie along the nominal entry trajectory. The angle of attack is near the equilibrium flight attitude. The jump in C_D just below $Re = 10^6$ is due to laminar turbulent transition in the vehicle wake and is also seen in the flight accelerometer records.

variations of C_D with Reynolds number and velocity shown in Figure 5 for continuum flow. The accuracy with which the drag coefficient was measured was within 1% (Appendix B).

For altitudes above 90 km the entry vehicle Reynolds number drops below 1000, and continuum flow gives way to slip flow. Near 115 km, free molecule flow begins. For this region we have not yet collected calibrating test data, although work is currently in progress to do so, and one preliminary measurement confirms the slip flow curve to within 5% at $Re = 460$. We have used literature values for the transitional regime from continuum to free molecule drag of spheres [*Masson et al.*, 1961] to model similarly the transition from laminar continuum $C_D = 1.47$ to an assumed value of 2.0 in free molecule flow, with Knudsen number as the governing parameter. Accordingly, the density results above 90 km are less accurate than those below 90 km.

Acceleration Data

The axial acceleration data from the two entries are shown in Figure 6. The accelerations were integrated on board the

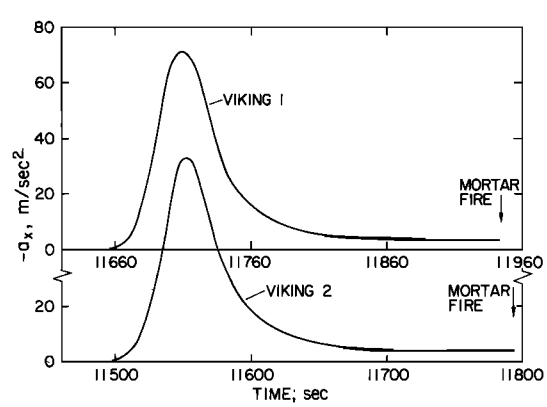

Fig. 6. Axial deceleration data. Time is measured from the instant of separation of the lander from the orbiter.

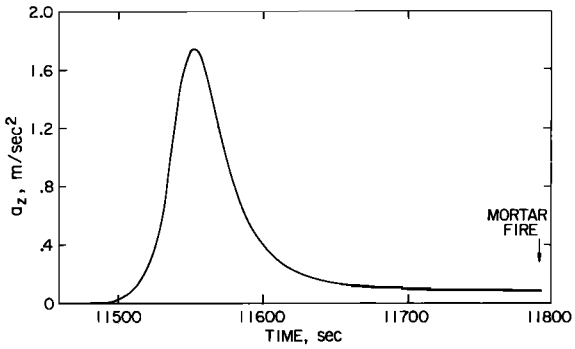

Fig. 7. Viking 2 z axis acceleration data.

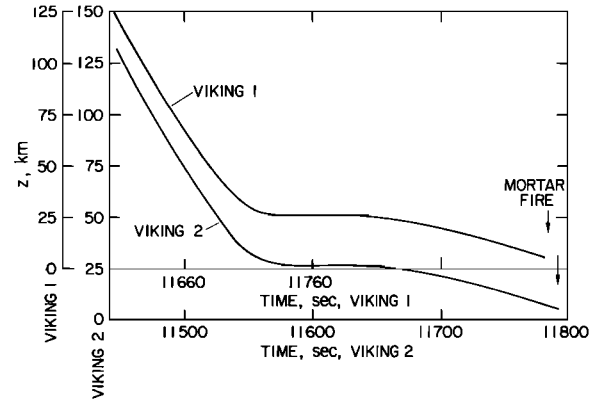

Fig. 9. Altitude data.

Viking landers and transmitted to earth as velocity pulse counts. Each axial pulse represented a velocity change of about 1.27 cm/s, and each lateral axis acceleration pulse about 0.32 cm/s. Atmosphere-relative velocities at entry (arbitrarily defined as an altitude of 244 km above the reference ellipsoid) were 4.418 and 4.477 km/s, respectively, for Viking 1 and 2, and so the axial velocity resolution provided was about 3 ppm of the entry velocity. At 10 samples/s the plotted data appear almost continuous. The peak axial deceleration, about 73 m/s² on Viking 2 and 71 m/s² on Viking 1, occurred at altitudes just above 30 km.

The z axis acceleration data, normal to x in the plane of the aerodynamic lift, are shown for Viking 2 in Figure 7. They essentially duplicate the shape of the axial deceleration profile but at a much lower level, peaking at 1.74 m/s². The ratio a_z/a_x is a measure of the aerodynamic lift-to-drag ratio and of the lander instantaneous angle of attack. The third component of acceleration, a_y, remained essentially zero.

From Figure 6 it can be seen that the axial acceleration threshold extends to at least 11490 s (Viking 2, z = 83 km), but at higher resolution it is seen to extend to appreciably higher altitude (Figure 8). At early times, less than one count/s is being measured, and the number alternates between adjoining levels, reflecting the fact that fractional values are being interpreted by a data system dealing only in integers. An 11-point running average of these data, representing the mean deceleration over an 11-s interval and plotted at the central point, produces the smoothed variation shown by the dots, which exhibit small scatter about the fitted line. The line, in turn, merges nicely with the values of instrument bias determined over long integration periods just prior to atmosphere entry. It is apparent that significant atmospheric decelerations are defined to an altitude near 125 km.

Altitude data from the altimeters on Viking 1 and 2 are shown in Figure 9. These data, at five samples/s, are also near continuous. They are uncorrected for variable terrain elevation and local roughness. These terrain characteristics can be extracted by detailed comparison of the altimeter data with the altitudes determined from the equations of motion analysis.

Both Viking entries, by virtue of their near glancing incidence relative to the atmosphere and the use of aerodynamic lift, experienced periods of essentially horizontal flight extending over about 50 km at altitudes near 28 km. It was found to be difficult to carry the atmosphere definition from the acceleration data through this region successfully, because of extreme sensitivity of the results to very small variations in the near-zero flight path angle and possibly also because of wind effects. We believe that we will be able to accomplish this, but it has not been done at this writing. Hence the accelerometric definition of the atmosphere presently terminates at the region where horizontal flight begins.

Atmospheric Profiles

The density data for the atmosphere of Mars derived from the accelerometer data of Viking 1 and 2 are given in Figure 10. Over the altitude range from about 28 to 120 km, the density ranges from 10^{-3} to 10^{-8} kg/m³ with a mean scale height of about 8 km but with significant curvature or waviness on the log ρ (z) plot, evidence of temperature variation

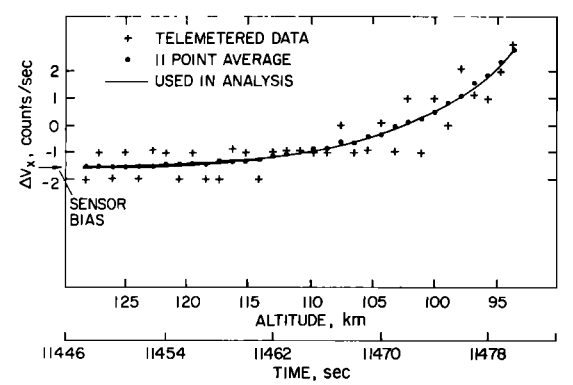

Fig. 8. Viking 2 axial velocity pulse counts near threshold. The telemetered data have been corrected for the small-velocity increments due to firing of the attitude control jets (note the occasional deviations from integral numbers of counts).

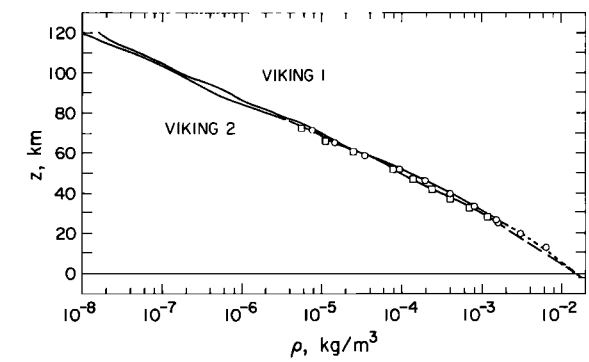

Fig. 10. Density profiles of Mars atmosphere to 120 km. Data shown by curved lines above 28 km are derived from accelerations. Points are from stagnation pressures (circles, Viking 1; squares, Viking 2). Densities from measured pressure and temperature during parachute descent are shown in the lowest 5 km.

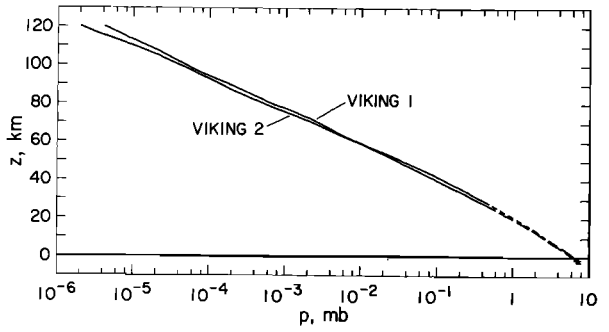

Fig. 11. Variation of pressure with altitude in Mars atmosphere. Above 28 km, pressure is derived from the density data, hydrostatic equilibrium being assumed; below 5 km, pressure is derived from direct sensing during parachute descent.

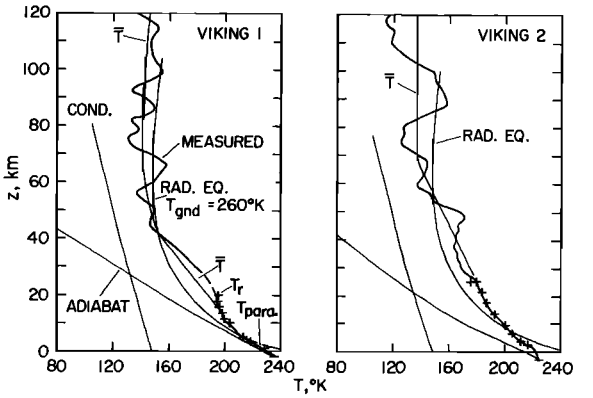

Fig. 12. Atmospheric temperature profiles below 120 km from Viking 1 and 2. The wave structure is the dominant characteristic. Comparisons are shown with the radiative equilibrium prediction of Gierasch and Goody and with an adiabatic profile. The condensation boundary lies well below the atmospheric temperatures. A curve which seeks to define the mean temperature $\bar{T}$ about which the oscillations are centered is indicated.

with altitude. Accuracy analysis indicates that the absolute accuracy of the densities should be within ~1% for the region of continuum aerodynamics, $z < 90$ km. At higher altitudes, present uncertainties in the drag coefficient in slip flow and free molecule flow could lead to errors of the order of 10%.

The pressure structure is plotted in Figure 11, and the temperature profiles in Figure 12. Since the data are essentially continuous, they are represented by lines rather than discrete points. Table 4 is a listing of the atmospheric state properties at 4-km intervals. The parachute phase direct-sensing data are included on these figures to show their relationship to the state properties determined by accelerometry and to define the atmosphere to ground level. In addition, the data obtained from aeroshell phase pressure and temperature sensing are included as symbols. These are described below.

The wave structure in the temperature profiles was identified in early discussions as evidence for strong thermal tidal oscillations in the atmosphere of Mars. The implications of these waves in relation to theory will be discussed in a later section.

Supporting Data From Aeroshell Phase Pressure and Temperature Sensing

The stagnation pressure readings taken throughout the high-speed entry are convertible to measurements of atmospheric density through the relation

$$C_{p_s} = (p_s - p_{atm})/(\tfrac{1}{2}\rho V_r^2) \tag{4}$$

wherein C_{p_s}, the stagnation pressure coefficient, is a theoretically known function of velocity (and weakly of gas composition), $p_s/p_{atm} \approx 500$ for $z > 35$ km (so that p_{atm} can be neglected in first approximation), and V_r is available from the trajectory reconstruction. The atmospheric densities derived from these independent data are plotted as symbols on Figure

TABLE 4. Atmosphere State Properties from Accelerometer Data

Altitude, km	Viking 1			Viking 2		
	ρ, kg/m³	p, mbar	T, °K	ρ, kg/m³	p, mbar	T, °K
120	1.60(−8)	4.14(−6)	136.3	8.86(−9)	1.99(−6)	116.0
116	2.42(−8)	6.91(−6)	149.2	1.69(−8)	3.76(−6)	115.5
112	3.95(−8)	1.12(−5)	148.6	3.08(−8)	6.98(−6)	118.2
108	6.59(−8)	1.84(−5)	146.4	5.62(−8)	1.30(−5)	121.1
104	1.06(−7)	3.03(−5)	149.4	9.36(−8)	2.35(−5)	131.8
100	1.67(−7)	4.94(−5)	154.8	1.42(−7)	4.01(−5)	147.9
96	2.88(−7)	8.02(−5)	145.9	2.30(−7)	6.60(−5)	150.2
92	5.39(−7)	1.38(−4)	133.6	3.63(−7)	1.08(−4)	155.1
88	8.33(−7)	2.33(−4)	146.7	5.79(−7)	1.74(−4)	157.5
84	1.40(−6)	3.87(−4)	144.2	1.06(−6)	2.88(−4)	141.4
80	2.57(−6)	6.70(−4)	136.6	2.11(−6)	5.08(−4)	126.1
76	4.66(−6)	1.16(−3)	130.5	3.83(−6)	9.22(−4)	125.9
72	7.70(−6)	2.05(−3)	139.1	6.71(−6)	1.68(−3)	130.9
68	1.17(−5)	3.43(−3)	152.9	1.07(−5)	2.91(−3)	143.0
64	1.88(−5)	5.55(−3)	154.6	1.82(−5)	4.94(−3)	142.3
60	3.19(−5)	9.11(−3)	149.5	3.26(−5)	8.54(−3)	137.3
56	5.96(−5)	1.56(−2)	136.8	5.27(−5)	1.47(−2)	146.4
52	9.56(−5)	2.67(−2)	146.3	8.23(−5)	2.46(−2)	156.5
48	1.57(−4)	4.45(−2)	148.6	1.20(−4)	3.92(−2)	170.7
44	2.65(−4)	7.46(−2)	147.5	1.94(−4)	6.19(−2)	166.8
40	4.10(−4)	1.23(−1)	157.4	3.14(−4)	9.87(−2)	164.5
36	6.25(−4)	1.98(−1)	166.1	5.04(−4)	1.58(−1)	164.4
32	9.32(−4)	3.12(−1)	175.1	7.92(−4)	2.54(−1)	167.6
28	1.38(−3)	4.83(−1)	183.8	1.22(−3)	4.04(−1)	173.2

Read 1.60(−8) as 1.60×10^{-8}.

10 and show very satisfactory agreement with those given by the accelerometers.

Although intuitively one would like to obtain atmospheric pressure from stagnation pressure data, (4) cannot be directly solved for p_{atm} without knowledge of ρ and hence of T_{atm}. That is, in the absence of independently obtained temperatures the equation cannot give directly more than a first approximation of the atmospheric pressure. It is evident, though, that p_{atm} can be obtained from ρ through integration of (14) in Appendix A and that if $\rho(z)$ from the stagnation pressure measurement agrees with that from the accelerometers, atmospheric pressures and temperatures will likewise agree.

The recovery temperature data taken during the aeroshell phase below a velocity of 1.1 km/s were used to define the temperature of the atmosphere in the altitude gap between the accelerometer and the parachute phase measurements. Since atmospheric specific heat is not constant over a broad range of temperatures, the solution proceeds through the enthalpies. The relation between recovery and ambient enthalpies is

$$h_{atm} = h_r + (V_r^2/2)[(1 - r)(V_l/V_r)^2 - 1] \qquad (5)$$

where h_r is the gas enthalpy at the recovery temperature, V_l is the local gas velocity incident on the sensor within the lander shock layer, and r is the recovery factor defined earlier. The temperatures from this analysis are shown in Figure 12 as the pluses between 3 and 25 km. The continuity of the data with the parachute phase direct sensing is good, and the data suggest that the wave structure of the temperature profile begins in this low-lying region, at initially small amplitudes.

MERGING OF THE ACCELEROMETER AND UPPER-ATMOSPHERE MASS SPECTROMETER DATA

Densities of the atmosphere above 120 km also were measured by the Viking Entry Science Team, by use of the upper-atmosphere mass spectrometer (UAMS) [*Nier et al.*, 1976; *Nier and McElroy*, 1976; *Nier and McElroy*, 1977]. The possibility was recognized well in advance of the Viking entries of joining these data with the accelerometer data to define the structure of the atmosphere from ground level to ~200 km, and it was with some eagerness that we compared the data to see the degree of compatibility that existed. This is shown in Figure 13.

To prepare this figure, the UAMS atmospheric number densities were converted to mass densities through the relation $\rho = \sum N_i\mu_i/N_A$, where N_i is the number density of species i, μ_i is its molecular weight, and N_A is Avogadro's number. (A. O. C. Nier has pointed out that we have a definition of Avogadro's number implicit in the data in regions of overlap of the UAMS and accelerometers.) To extend the data to the highest altitudes, it was necessary to extrapolate number densities of some of the minor species. Furthermore, an allowance was made for the presence of atomic oxygen, based on the observation by *Hanson et al.* [1977] that a number density of 5×10^8 was indicated for an altitude of 135 km on Viking 1. This observation was extended upward by assuming that the O was in hydrostatic equilibrium, at the same temperature as the other neutral constituents. The implied assumption is that there are no chemical reactions acting as a major source or sink for O in this altitude range, which may not be the case. With this assumption, atomic oxygen becomes an important bulk constituent above about 150 km, rising to a mole fraction of 0.4 at 170 km. Neglecting the O fraction would not, however, change the essential character of the $\log \rho(z)$ plot. The densities would be shifted downward by about 15% at 170 km, a small shift on the logarithmic plot. (The small effect of O on mass density is due to its low molecular weight relative to those of other species present.)

The UAMS density points, although more widely spaced, exhibit a curvature with altitude on the semilogarithmic plot similar to that shown by the accelerometer-derived densities. (Because of the relatively wide point spacing, some of the fine structure may be lost.) Furthermore, it is possible to join data from the two instruments without any discontinuities in density or its gradient if the curve is not forced through the last data point from each instrument. There is excellent reason to give these last-obtained points low weight. For the accelerometry the reason is that the measurement is near threshold, where accuracy is diminishing, and is in free molecule flow, where C_D is more uncertain. For the UAMS the reason is that the instrument is becoming saturated by the high inlet flux, and the calibration is less certain; also, if the transition to continuum flow has begun, the ground test data obtained in the molecular beam cannot give the ratio between measured and free stream densities reliably. It is evident that the joining of these two sets of data was very satisfactory, and in combination they define the density profile essentially from ground level to nearly 200 km.

The density profiles were used to derive pressures and temperatures as described earlier, by means of (14) and the equation of state, with the results shown in Figures 14 and 15. Values of the state properties derived from the UAMS data are

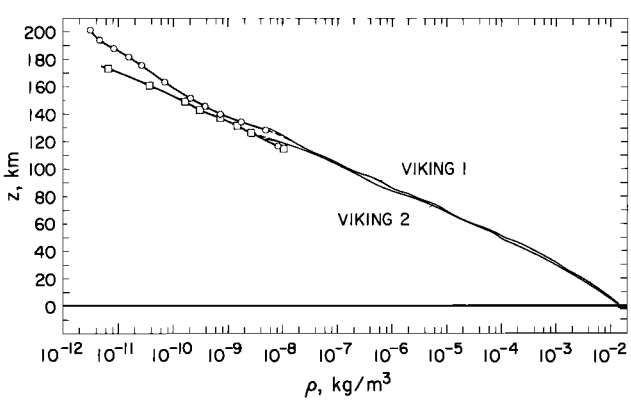

Fig. 13. Density profiles from ground level to 200 km obtained by merging the mass spectrometer and accelerometer density data. The merging altitude is around 120 km. Differences between the Viking 1 and Viking 2 soundings are the combined result of differences in latitude, season, and time of day. Viking 1 landed at 22.3°N at 4:13 P.M. MLT on July 20, 1976, Viking 2 at 47.7°N at 9:49 A.M. MLT on September 3, 1976.

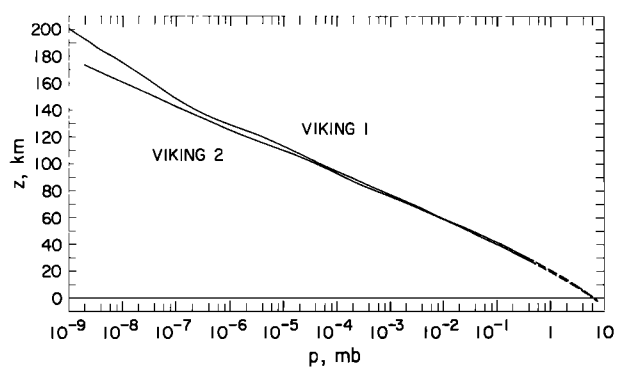

Fig. 14. Pressure structure of Mars atmosphere to 200 km derived from measured density profiles of Figure 13.

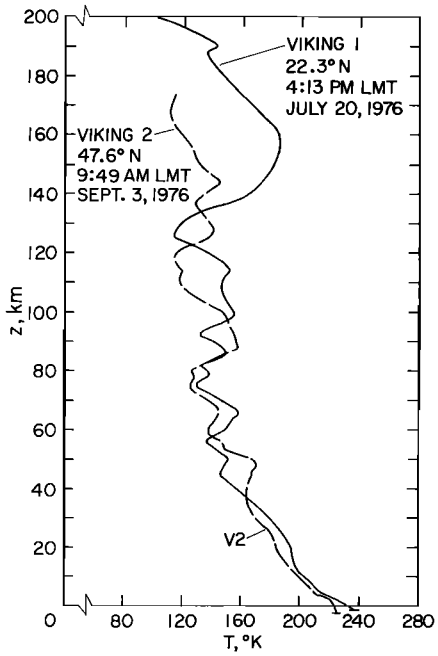

Fig. 15. Temperature of the neutral atmosphere from synthesis of all available entry science data.

listed in Table 5. The mean molecular weight was allowed to vary with altitude in the fashion shown by the UAMS data. The wave structure determined below 120 km continues upward in a continuous fashion, increasing in both wavelength and amplitude with increasing altitude.

Our procedure for deriving the temperatures differs from that used by *Nier and McElroy* [1977] in several respects. First, it is applied to the smoothed density variation indicated by the total set of data, including the merging of the accelerometer densities with the UAMS densities, rather than being a linear, point-to-point type of calculation. (We make no assumption of local linearity.) Second, it uses the total atmospheric density as a basis rather than the number density of CO_2 alone. Nevertheless, the temperatures from the two analyses agree within 10° or 15° below 160 km but diverge at higher altitudes, although our values are generally within the uncertainty bars which they have indicated.

It should be explained that the starting temperature at the highest altitude depends on the starting pressure, which in turn depends on the column density above that altitude. Since this was not experimentally determined, the starting temperature was fixed by fitting a straight line to the uppermost 10 km of the density curve to define the scale height and hence the temperature at that level, which was used with the measured density and composition to compute the starting pressure.

COMPARISON OF ATMOSPHERE STRUCTURE FROM VIKING 1 AND 2 ENTRIES

The atmosphere density data from Viking 1 and 2 are compared in Figure 13. The first-order conclusion is that they are closely similar. In the lower atmosphere, below 50 km, densities seen by Viking 2 were as much as 28% lower than those seen by Viking 1. The two profiles come together around 60 km and approach closely near 100 km before diverging strongly above 100 km. Near the surface, Figure 4 showed larger densities for Viking 2 than for Viking 1, but if the difference in landed elevation is taken into account, then at the reference ellipsoid, $\rho_{0_{V1}}$ (0.0150 kg/m³) is essentially equal to $\rho_{0_{V2}}$ (0.0148 kg/m³).

It is natural to inquire whether these density profiles satisfy the observed surface pressure differences through the equation of hydrostatic equilibrium. The answer is yes, since hydrostatic equilibrium has been assumed in interpreting the accelerometer data, and it has been shown that for both sets of data an equation of the form $p/p_0 = \exp(-z/H)$ (representing isothermal hydrostatic equilibrium) fits the near-surface data well. Between 5 and 30 km, temperature variations with altitude require only that the scale height vary slightly with altitude.

Since 95% of the pressure at any altitude is contributed by the mass of gas within 3 scale heights upward, one might expect to find differences in pressure between Viking 1 and 2 that are greater at higher altitudes than those at the reference surface, where the difference is 6.7%. This proves to be the case, as shown in Figure 14. A pressure difference of ~15% of the mean occurs, for example, at 35 km. At 58 km, however, pressures from the two soundings were within 4%.

If these data were simultaneous, they would indicate a strong driving potential for atmosphere circulation at some altitudes. However, they are not simultaneous, and so a

TABLE 5. Mass Densities, Pressures, and Temperatures Derived from UAMS Data

Viking 1				Viking 2			
Altitude, km	ρ, kg/m³	p, mbar	T, °K	Altitude, km	ρ, kg/m³	p, mbar	T, °K
200	3.30(−12)	1.05(−9)	102	174	5.80(−12)	1.93(−9)	115
195	4.70(−12)	1.67(−9)	125	170	1.07(−11)	3.06(−9)	112
190	6.62(−12)	2.53(−9)	143	166	1.90(−11)	5.04(−9)	112
185	1.13(−11)	4.02(−9)	139	162	3.23(−11)	8.46(−9)	116
180	1.80(−11)	6.48(−9)	148	160	4.15(−11)	1.10(−8)	119
175	2.77(−11)	1.03(−8)	158	156	6.82(−11)	1.83(−8)	125
170	4.21(−11)	1.61(−8)	167	152	1.13(−10)	3.05(−8)	129
165	6.27(−11)	2.48(−8)	177	148	1.81(−10)	5.04(−8)	135
160	9.35(−11)	3.78(−8)	186	144	2.75(−10)	8.15(−8)	145
155	1.48(−10)	5.80(−8)	185	140	4.90(−10)	1.33(−7)	135
150	2.41(−10)	9.05(−8)	182	136	8.65(−10)	2.24(−7)	130
145	4.10(−10)	1.45(−7)	175	132	1.43(−9)	3.81(−7)	136
140	7.25(−10)	2.39(−7)	166	128	2.31(−9)	6.36(−7)	141
135	1.59(−9)	4.21(−7)	136				
130	3.80(−9)	8.77(−7)	120				

Read 3.30(−12) as 3.30×10^{-12}.

primary difference to be considered is the effect of seasonal condensation of the atmosphere [*Hess et al.*, 1976*b*]. Approximately 7.35% of the atmosphere of Mars condensed between the landings of Viking 1 and 2. Thus the pressure difference between the two soundings oscillates about this mean reduction.

Very sizable pressure differences are indicated between the two entries at altitudes above 100 km, e.g., a factor >2 at 150 km and a factor >5 at 170 km. Pressure differences of this magnitude are suggestive of very strong circulations in the upper atmosphere of Mars. These differences are a consequence of the lower temperatures, hence smaller scale heights, of the Viking 2 upper atmosphere, which lead to increasing differences in density with altitude. Thus the number densities of CO_2 at 170 km are 4.9×10^8 (Viking 1) and 1.04×10^8 (Viking 2) [*Nier and McElroy*, 1977]. Pressure is then lowered because of both density and temperature, but ultimately, the lower temperature is the cause.

A comparison of the temperature profiles is given in Figure 15. The remarkable thing that emerges is the very close correspondence of the two profiles. We were fully expecting to find significant effects of the change in season and latitude, both of which should tend to lower Viking 2 temperatures relative to those of Viking 1. The data show that their combined effect is to lower temperatures a few degrees at altitudes from 5 to 35 km and to lower the mean temperature 4°–10° up to 120 km. A larger effect on mean temperature is seen above 120 km, where the mean appears to be about 126° for Viking 2, compared to 150° for Viking 1. In the intermediate altitudes, 35–100 km, the major differences appear to be due primarily to the phase and modal makeup of the diurnal oscillation and not to differences in the mean.

The upper-atmospheric temperature difference appears to be a result of one large dynamic half-wave extending from 135 km to upward of 185 km. Thus the difference in mean temperature may be a consequence of more vigorous dynamic oscillations at the near subsolar Viking 1 site. However, the direct solar heating of the upper atmosphere should also be greater at this location, and a diurnal effect (late afternoon versus early morning) may also contribute to the difference in upper-atmospheric temperatures.

In the lowest 5 km there is the diurnal difference referred to earlier. Thus we can summarize three differences between the temperature profiles at the two landing sites: (1) diurnal differences near the surface, (2) a small temperature difference (~3°–10°) below 35 km and in mean temperature up to 120 km due to season and latitude, and (3) a 25° temperature difference above 120 km, possibly controlled by dynamics.

It will now be of interest to compare these findings with pre-Viking theoretical expectations.

COMPARISONS WITH THEORY, THEORETICAL IMPLICATIONS

Mean Temperature Profiles

Processes governing the temperature profiles in the atmosphere of Mars were studied theoretically by *Gierasch and Goody* [1967, 1968]. In the 1967 paper (paper A) they calculate radiative equilibrium profiles, and in the 1968 paper (paper B) they incorporate effects of free convection and the diurnal radiative wave emanating from the surface, while arguing that planetary-scale circulation is not a first-order consideration in determining temperatures. Although dynamical oscillations were not treated, they were alluded to as a possibly significant phenomenon for Mars.

We will not attempt a quantitative comparison with this theory, simply because the cases calculated and presented do not coincide closely with conditions of season, latitude, and ground temperature actually encountered by the Viking landers. However, it is possible to examine the theory relative to the observations and to draw some conclusions. The first concerns the important role of radiative equilibrium.

The radiation equilibrium temperature profile for a clear (dust free) atmosphere (interpolated from paper A for a ground temperature of 260°) gives a first-order representation of the mean profiles observed (Figure 12). The differences between the calculated and observed (mean) profiles could possibly be explained by the presence of dust in the lower atmosphere, which would be expected to warm the dust-carrying levels while shielding the higher levels from ground radiation to some degree. They could also be explained by an underestimate of atmospheric radiative absorption.

The major effect of a dust storm on the temperature profiles was well displayed during the early stages of the Mariner 9 mission [*Hanel et al.*, 1972; *Kliore et al.*, 1972]. *Gierasch and Goody* [1971] showed that an absorption of 0.1 of the solar heating by dust in the atmosphere would modify their results to agree with the Mariner 9 data during the height of the storm. During the entries of the Viking landers the atmosphere was quite transparent, but there was evidence for a small dust fraction, seen in the scattering of sunlight to produce a pink sky [*Mutch et al.*, 1976].

The Viking 1 entry at 4:15 P.M. was at the time of day for which paper B predicts a sharply defined tropopause at altitudes near 15 km, with essentially adiabatic lapse below that. This type of structure, predicted for winter and summer mid-latitudes and for the equatorial region at equinox, was not encountered by the Viking landers.

Below about 5 km the radiative equilibrium temperature profiles are unstable, for T_{gnd} = 260°K, and should give way to a region of adiabatic temperature lapse. Experimentally, the lapse rate remains stable, in both the late afternoon and morning profiles, down to the lowest altitude of observation, 1.5 km. Linear extension of the measured temperature profiles to the ground agrees with the landed temperatures, sensed on sol 1 at the same time of day, to within 2.5° on Viking 1 and 1.5° on Viking 2. If these comparisons are error free, they would admit an adiabatic lapse region in the lowest 1.5 km of Viking 1 and the lowest 0.4 km of Viking 2.

However, there is a clear change in slope of the profiles a few kilometers above the surface, especially in the Viking 1 profile at 4 km, which suggests that a convective region occurs near the surface. Since the temperature profile does not admit natural (thermal) convection, the data suggest the presence of turbulent forced convection due to winds and a boundary layer thickness of 6 km, extending to 4 km above the reference ellipsoid. In the boundary layer the temperatures are near adiabatic, indicating the occurrence of vertical mixing, while above it they veer sharply away from the adiabat. Since potential temperature increases with height in the boundary layer, the forced convection transports heat downward.

Forced convection can explain an adiabatic profile, but some further explanation is needed for the subadiabatic profiles observed. *Stone* [1972] has indicated that stable lapse rates will occur in winds driven by baroclinic instability. *Blumsack et al.* [1973] incorporate an empirical dynamic vertical heat flux term in their model and present an example in which the lapse rate becomes subadiabatic roughly 1 scale height above the surface. Perhaps these kinds of processes are responsible

TABLE 6. Measured Characteristics of the Temperature Wave Structure

Peak No.	Viking 1				Viking 2			
	z, km	ΔT, °K	Δz, km	λ, km	z, km	ΔT, °K	Δz, km	λ, km
1	44.5	−3.5	+0.75	11	33	−5	+1.2	31
2	50	+4	−1.0	12	48.5	+14.5	−3.4	22
3	56	−7	+1.7	20	59.5	−8	+1.8	16
4	66	+17	−4.2	20	67.5	+6.5	−1.5	13
5	76	−10	+2.2	6	74	−10.5	+2.4	8
6	79	−2.5	+0.7	6	78	−9	+2.0	4
7	82	−8	+1.8	9	80	−10	+2.1	17
8	86.5	+6	−1.6	12	88.5	+21.5	−5.3	15
9	92.5	−9	+2.1	14	96	+14	−3.6	8
10	99.5	+12	−3.2	17	100	+12	−2.8	20
11	108	+2.5	−0.9	13	110	−18.5	+4.2	8
12	114.5	+7.5	−1.8	23	114	−17	+3.7	8
13	126	−32	+7.5	68	118	−22	+4.9	19
14	160	+40	−12.4		127.5	+5	−1.3	18
15					136.5	−7.5	+1.8	15
16					144	+9	−2.4	46
17					167	−25	+7.0	

for stable lapse rates in the lowest 5 or 6 km of Mars atmosphere.

The effect of the ground temperature cycle in cooling the atmosphere during the night and warming it during the day was predicted in paper B to be limited to the lowest levels of the atmosphere, having little effect above 5 km and large effect only below 2 km. This phenomenon is seen in the comparison of Viking 1 and 2 near-surface data to extend up to ~4 km above the surface, and it is apparently very much as anticipated. The heat exchange is radiative, so that dust in the atmosphere would perhaps be expected to enhance and extend the region of diurnal variation in temperature.

The CO_2 condensation boundary has been included in Figure 12. In both the morning and late afternoon profiles there is a minimum margin of ~20°K between atmospheric temperature and condensation. In view of the lack of diurnal variation of the mean profile above the boundary layer it appears that only a large negative amplitude of the thermal tide could condense CO_2 and that hazes and clouds seen in the Mars atmosphere in the summer season below polar latitudes are most probably water ice.

Wave Structure

We have previously discussed the relationship of the wave structure in the Viking 2 temperature profile to the tidal model of *Zurek* [1976] [*Seiff and Kirk,* 1976]. The Viking 1 wave structure is generally similar to that of Viking 2, with differences in phase and amplitude associated with latitude and time of day (Figure 15). The waves appear to be a complex superposition of modes. Table 6 lists approximately the temperature amplitudes and wavelengths obtained relative to the mean temperature curve drawn through the data (Figure 12). The wavelengths are measured over half a cycle, from one peak to the next higher peak. The significance of the Δz column will be explained below.

The wavelength varies from 4 to 31 km below 100 km and grows to a maximum in the uppermost half cycle of each sounding. For comparison the theoretical model has indicated wavelengths of 22–24 km. The wavelength values depend, of course, on just how small a disturbance is considered to define a peak. For example, the Viking 2 'peaks' at 78 km and 96 km, which lead to two of the smaller wavelengths, are of very small amplitude. Their omission from Table 6 would increase λ at 74 km to 12 km and at 88.5 km to 23 km. They are suggestive of a tendency for a minor peak to appear from a mode locally out of phase with the fundamental mode. The reality of these details is not clear to us, but we are interpreting them literally, as measured. The most prominent of these out-of-phase peaks is at 79 km on Viking 1.

There appear to be two or three peaks (not included in the table) in the wave structure of the Viking 1 sounding below the 45-km peak. These suggest that the wave structure persists down to the level of the boundary layer edge. The temperature amplitude is initially small (a few degrees), then increases with altitude to the order of 15° or 20°, then is damped somewhat before increasing to very large values above 100 km.

Zurek has calculated that horizontal velocities excited by the diurnal heating cycle are as large as 150 m/s, above 70 km, under clear air conditions. Vertical flow velocities are about 2 orders less, up to 1.5 m/s. If adiabatic compression and expansion resulting from the vertical flow component are assumed to be responsible for the temperature waves, the amount of vertical movement thus implied by the observed peaks is given in Table 6 under the heading Δz. Vertical excursions of a few kilometers are sufficient to produce the observed temperature structure. Vertical motion at 0.1 m/s can account for the smaller displacements in 4 hours (1.44 km), while 1 m/s for 4 hours (14.4 km) would account for the largest displacement. These velocity magnitudes are compatible with the theoretical model.

Horizontal winds of the magnitude described, in the presence of wind shear, can be expected to break down into turbulence and to contribute to mixing of the atmosphere. The larger velocities and greater range of motion observed at the higher altitudes suggest a more vigorous turbulent mixing there. The possible relationship of this dynamical turbulent mixing process to the observed photochemical stability of the atmosphere has been pointed out by Zurek and others.

Finally, Zurek has discussed the effect of terrain on tidal oscillations and concludes that it will have first-order effects, adding modes and varying the contributing modes with longitude. We suspect that some of the modal complexity observed in our data is the effect of the terrain, which for Viking 1 was a rapidly descending rolling surface, near the center of a deep

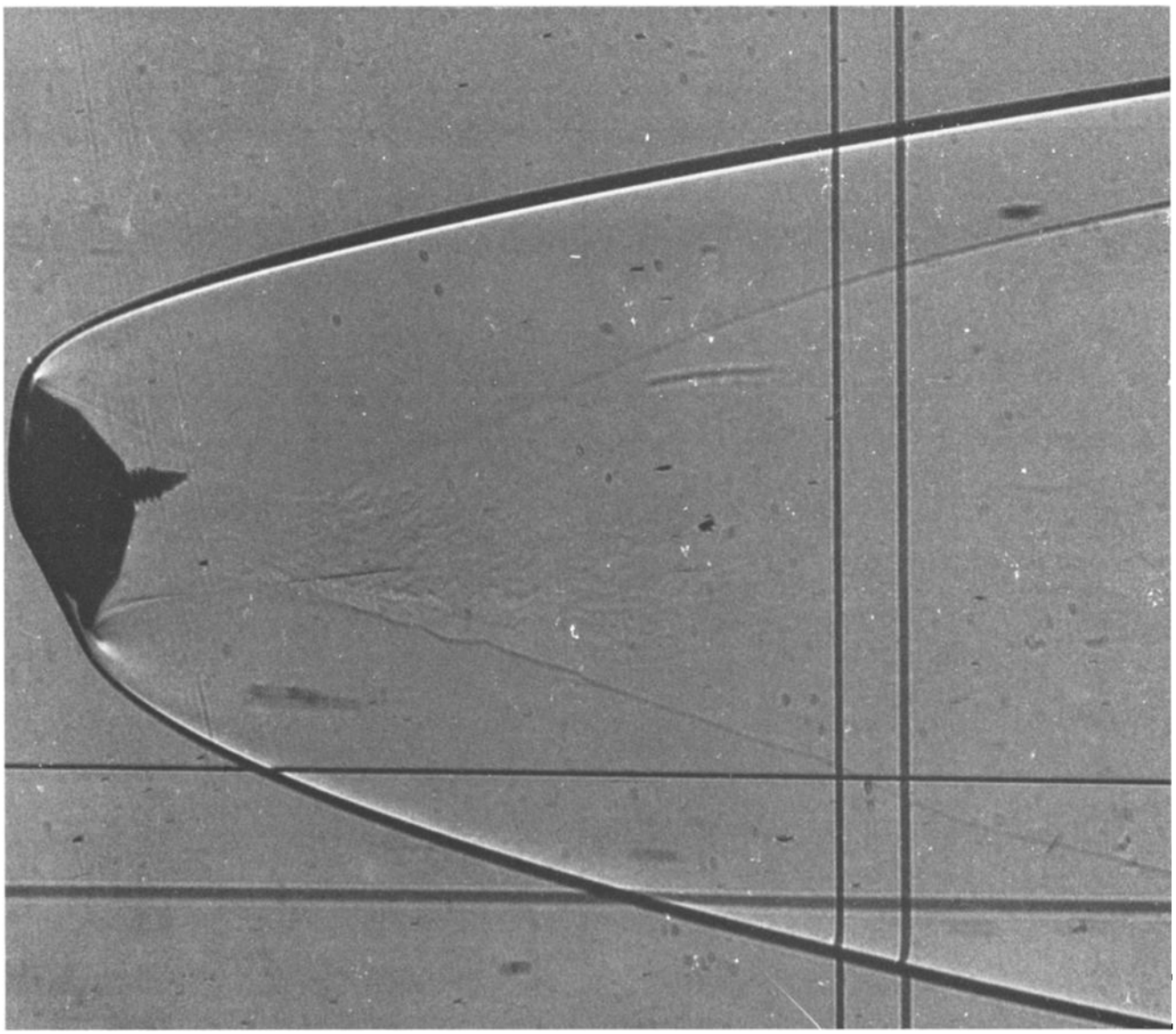

Fig. 16. Shadowgraph of a model of the Viking entry configuration in a laboratory test flight. The atmosphere is CO_2, the model's velocity is 3.4 km/s, and the Reynolds number is 8×10^5. In this figure the model is at the Viking equilibrium flight attitude, $\alpha \approx -11°$.

basin. The theory shows that low basins enhance the velocities and the temperature amplitude (see, for example, the results for 120°W longitude, at the equator and at 19°N, in *Zurek*'s [1976] paper).

APPENDIX A: DATA ANALYSIS

The equations of motion used to reconstruct the trajectory were as follows:

Inertial velocity

$$dV_I/dt = g \sin \gamma_I - a_{s_I} \tag{6}$$

Resolution of accelerations

$$a_{s_I} = (a_x \cos \alpha + a_z \sin \alpha) \cos \epsilon_1 - (a_x \sin \alpha - a_z \cos \alpha) \cos \epsilon_2 \tag{7}$$

$$a_{L_I} = -(a_x \sin \alpha - a_z \cos \alpha) \cos \epsilon_3 + (a_x \cos \alpha + a_z \sin \alpha) \cos \epsilon_4$$

where ϵ_1 is the angle between V_I and V_r; ϵ_2, the angle between V_I and L_r; ϵ_3, the angle between L_I and L_r; and ϵ_4, the angle between L_I and V_r. L_I and L_r are the lift vectors perpendicular to V_I and V_r, respectively. Subscript I denotes an inertial reference frame, and subscript r denotes a reference frame anchored in the atmosphere rotating with the planet. Note that ϵ_1 and $\epsilon_3 \approx 0°$, while ϵ_2 and $\epsilon_4 \approx 90°$.

Inertial flight path angle

$$d\gamma_I/dt = -\{[V_I/(R + z)] - (g/V_I)\} \cos \gamma_I + (a_{L_I}/V_I) \tag{8}$$

Gravitational acceleration

$$g = g_0 R^2/(R + z)^2 \tag{9}$$

Altitude

$$dz/dt = -V_I \sin \gamma_I \tag{10}$$

Downrange angle

$$d\delta/dt = (V_I \cos \gamma_I)/(R + z) \tag{11}$$

Relative velocity

$$V_r^2 = V_I^2 + V_a^2 - 2V_I V_a \cos \gamma_I \sin \lambda_I \tag{12}$$

Velocity of atmosphere rotating with planet

$$V_a = (R + z)\,\omega \cos \Phi \tag{13}$$

Hydrostatic equilibrium

$$dp/dt = g\rho V_I \sin \gamma_I \tag{14}$$

Here, a_{s_I} is the acceleration in the V_I direction, R is the local radius of the planet (measured to the reference ellipsoid), γ_I is the flight path angle below horizontal, α is the angle of attack, δ is the range angle subtended at the planet center from entry to time t, λ_I is the trajectory heading angle (0° is due north), ω is planetary rotation rate ($7.08821765 \times 10^{-5}$ rad/s), and Φ is latitude.

The data analysis was programed for computer solution. The acceleration and altitude data were processed by the program to yield the trajectory and the properties of the atmosphere. The iterative procedure used follows.

1. First approximations of the initial conditions (inertial velocity, flight path angle, altitude, latitude, and heading angle) are made on the basis of the expected, or mission nominal, trajectory. These conditions are for a selected arbitrary time prior to encountering the sensible atmosphere.
2. A table of altitudes measured by the radar altimeter is stored in memory as a function of time.
3. Differential equations (6) and (8) are solved simultaneously, supported by auxiliary equations (7) and (9). Altitudes are calculated for each of the times specified in step 2. (Note that in (7), a_x and a_z are the measured accelerations and that the angle of attack, α, is calculated from their ratio through the experimentally determined lift and drag coefficients.)
4. When a specified final altitude is reached, a differential corrections process [*Chapman and Kirk*, 1970] is applied to yield corrections to the initial conditions. This involves solving another set of differential equations in which partial derivatives of velocity, flight path angle, etc., with respect to the initial conditions, are determined. Given a new set of initial conditions, the process is repeated until a best fit in a least squares sense is obtained to the altitude data. Normally three or four iterations lead to convergence.
5. Relative velocity is determined as a function of time from (12), and the density is then determined from (3). Pressure and temperature are computed from the assumption of hydrostatic equilibrium (equation (14)) and from the gas law. The mean molecular weight used for the mixed lower atmosphere in this step was 43.49, corresponding to 2.7 mol % N_2, 1.6 mol % Ar, and 0.15 mol % O_2.

APPENDIX B: DRAG COEFFICIENT DETERMINATION

Continuum flow drag coefficients were measured in a series of experiments conducted at Ames Research Center in a ballistic range with CO_2 as the test medium [*Intrieri et al.*, 1977; P. F. Intrieri, personal communication, 1976]. The tests were designed to define the effects of gas composition, angle of attack, Reynolds number, and velocity on drag coefficient. Accurately made scale models of the Viking entry configuration were fired from light-gas guns through an atmosphere of carbon dioxide in an enclosed test range, at velocities and Reynolds numbers selected to lie along the Viking entry trajectory. Reynolds number was controlled by selection of gas pressure within the test range. Drag coefficients were determined from precise measurements of the model retardation in flight (see, for example, *Canning et al.* [1970]). In addition, the lift, static and dynamic stability, and trim angle of attack were determined.

A shadowgraph picture of one of the models in flight is reproduced in Figure 16 to show the flow configuration typical of the high entry speeds and attitude. An example of the drag data is given in Figure 17. It shows the accuracy of the data to be within 1%. The effect of angle of attack is well defined. The comparison with air data shows a 4% effect on C_D of the change in gas composition at the flight attitude. Test data for CO_2, slightly contaminated by air leakage, were used in reducing the Viking flight data. A more complete report of these tests is planned.

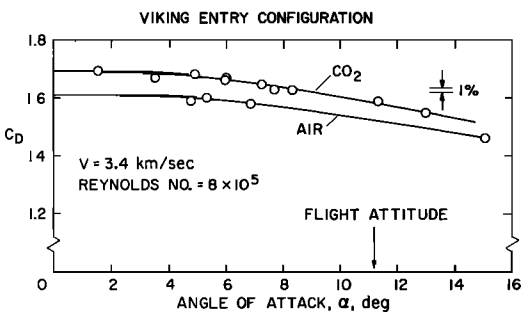

Fig. 17. Representative data from laboratory measurements of drag coefficient.

Acknowledgments. The authors are indebted to many people who, over the years of preparation of this experiment, contributed significantly to its development, implementation, and analysis. Unfortunately, we cannot acknowledge all who contributed here, but in particular we wish to thank Robert C. Blanchard of the Langley Research Center Viking Project Office (VPO) and Fred Hopper of Martin Marietta Corporation (MMC) for invaluable contributions to the trajectory reconstruction effort; Simon C. Sommer and David E. Reese of Ames Research Center (ARC) for major contributions to the demonstration of the concept; Robert Corridan and Carlton S. James (ARC) for laboratory studies of the instruments; and Roy Duckett and Brooks Drew (VPO) and Sid Cook, Tony Knight, and Ernie Carlston (MMC) for contributions to the experiment integration in the spacecraft and operations planning; and finally, Roland Dupree (Kennedy Space Center) and Sally Rogallo (ARC) for invaluable assistance in the computer analysis of the flight data.

REFERENCES

Blumsack, S. L., P. J. Gierasch, and W. R. Wessel, An analytical and numerical study of the Martian planetary boundary layer over slopes, *J. Atmos. Sci.*, *30*, 66–82, 1973.

Canning, T. N., A. Seiff, and C. S. James (Eds.), Ballistic range technology, *Rep. 138*, Adv. Group for Aeronaut. Res. and Develop., Brussels, 1970.

Chapman, G. T., and D. B. Kirk, A method for extracting aerodynamic coefficients from free flight data, *AIAA J.*, *8*, 753–758, 1970.

Christensen, E. J., Martian topography derived from occultation, radar, spectral, and optical measurements, *J. Geophys. Res.*, *80*, 2909–2913, 1975.

Gierasch, P. J., and R. M. Goody, An approximate calculation of radiative heating and radiative equilibrium in the Martian atmosphere, *Planet. Space Sci.*, *15*, 1465–1477, 1967.

Gierasch, P. J., and R. M. Goody, A study of the thermal and dynamical structure of the Martian lower atmosphere, *Planet. Space Sci.*, *16*, 615–646, 1968.

Gierasch, P. J., and R. M. Goody, The effect of dust on the temperature of the Martian atmosphere, *J. Atmos. Sci.*, *29*, 400–402, 1971.

Hanel, R., B. Conrath, W. Hovis, V. Kunde, P. Lowman, W. Maguire, J. Pearl, J. Pirraglia, C. Prabhakara, and B. Schlachman, Investigation of the Martian environment by infrared spectroscopy on Mariner 9, *Icarus*, *17*, 423–442, 1972.

Hanson, W. B., S. Sanatani, and D. R. Zuccaro, The Martian ionosphere as observed by the Viking retarding potential analyzers, *J. Geophys. Res.*, *82*, this issue, 1977.

Hess, S. L., R. M. Henry, C. B. Leovy, J. A. Ryan, J. E. Tillman, T. E. Chamberlain, H. L. Cole, R. G. Dutton, G. C. Greene, W. E. Simon, and J. L. Mitchell, Preliminary meteorological results on Mars from the Viking 1 lander, *Science*, *193*, 788–791, 1976*a*.

Hess, S. L., R. M. Henry, C. B. Leovy, J. A. Ryan, J. E. Tillman, T. E. Chamberlain, H. L. Cole, R. G. Dutton, G. C. Greene, W. E. Simon, and J. L. Mitchell, Mars climatology from Viking 1 after 20 sols, *Science, 194*, 78–81, 1976*b*.

Intrieri, P. F., C. E. De Rose, and D. B. Kirk, Flight characteristics of probes in the atmospheres of Mars, Venus, and the outer planets, *Acta Astronaut.*, in press, 1977.

Kerzhanovich, V. V., Mars 6: Improved analysis of the descent module measurements, *Icarus, 30*, 1–25, 1977.

Kliore, A. J., D. L. Cain, G. Fjeldbo, B. L. Seidel, and M. J. Sykes, The atmosphere of Mars from Mariner 9 radio occultation measurements, *Icarus, 17*, 484–516, 1972.

Masson, D. J., D. N. Morris, and D. E. Bloxsom, Measurements of sphere drag from hypersonic continuum to free-molecule flows, in *Rarified Gas Dynamics*, edited by L. Talbot, p. 643, Academic, New York, 1961.

Michael, W. H., Jr., A. P. Mayo, W. T. Blackshear, R. H. Tolson, G. M. Kelly, J. P. Brenkle, D. L. Cain, G. Fjeldbo, D. N. Sweetnam, R. B. Goldstein, P. E. MacNeil, R. D. Reasenberg, I. I. Shapiro, T. I. S. Boak, M. D. Grossi, and C. H. Tang, Mars dynamics, atmospheric, and surface properties: Determination from Viking tracking data, *Science, 194*, 1337–1338, 1976.

Mutch, T. A., A. B. Binder, F. O. Huck, E. C. Levinthal, S. Liebes, Jr., E. C. Morris, W. R. Patterson, J. B. Pollack, C. Sagan, and G. R. Taylor, The surface of Mars: The view from the Viking 1 lander, *Science, 193*, 791–801, 1976.

Nier, A. O., and M. B. McElroy, Structure of the neutral upper atmosphere of Mars: Results from Viking 1 and Viking 2, *Science, 194*, 1298–1300, 1976.

Nier, A. O., and M. B. McElroy, Composition and structure of Mars upper atmosphere: Results from the neutral mass spectrometers on Vikings 1 and 2, *J. Geophys. Res., 82*, this issue, 1977.

Nier, A. O., W. B. Hanson, M. B. McElroy, A. Seiff, and N. W. Spencer, Entry science experiments for Viking, 1975, *Icarus, 16*, 74–91, 1972.

Nier, A. O., W. B. Hanson, A. Seiff, M. B. McElroy, N. W. Spencer, R. J. Duckett, T. C. D. Knight, and W. S. Cook, Composition and structure of the Martian atmosphere: Preliminary results from Viking 1, *Science, 193*, 786–788, 1976.

Owen, T., and K. Biemann, Composition of the atmosphere at the surface of Mars: Detection of argon 36 and preliminary analysis, *Science, 193*, 801–803, 1976.

Seiff, A., Some possibilities for determining the characteristics of the atmospheres of Mars and Venus from gas dynamic behavior of a probe vehicle, *NASA Tech. Note, D-1770*, 1963.

Seiff, A., The Viking atmosphere structure experiment—Techniques, instruments, and expected accuracies, *Space Sci. Instrum., 2*, 381–423, 1976.

Seiff, A., and D. B. Kirk, Structure of Mars' atmosphere up to 100 km from the entry measurements of Viking 2, *Science, 194*, 1300–1303, 1976.

Seiff, A., D. E. Reese, S. C. Sommer, D. B. Kirk, E. E. Whiting, and H. B. Niemann, Paet, An entry probe experiment in the earth's atmosphere, *Icarus, 18*, 525–563, 1973.

Stone, P. H., A simplified radiative-dynamical model for the static stability of rotating atmospheres, *J. Atmos. Sci., 29*, 405–418, 1972.

Zurek, R. W., Diurnal tide in the Martian atmosphere, *J. Atmos. Sci., 33*, 321–337, 1976.

(Received April 13, 1977;
revised June 6, 1977;
accepted June 6, 1977.)